# Giant multipole resonances from inelastic scattering of 152-MeV alpha particles

F. E. Bertrand, G. R. Satchler, D. J. Horen, and J. R. Wu
*Oak Ridge National Laboratory, Oak Ridge, Tennessee 37830*

A. D. Bacher, G. T. Emery, W. P. Jones, and D. W. Miller
*Indiana University, Bloomington, Indiana 47401*

A. van der Woude
*Kernfysisch Versneller Instituut, Groningen, The Netherlands*

(Received 12 May 1980)

Giant resonance spectra have been measured for $^{208}$Pb, $^{120}$Sn, $^{90}$Zr, $^{58}$Ni, and $^{46}$Ti, using inelastic scattering of 152-MeV alpha particles. In addition to some low-lying states, the spectra were analyzed to yield separate peaks for the giant quadrupole resonance and giant monopole resonance, except in $^{46}$Ti, where no evidence was found for a giant monopole resonance. The results for the monopole resonance when compared to distorted-wave Born-approximation calculations show that $\sim 100\%$ ($\pm 20\%$) of the $T=0$, $L=0$ energy weighted sum rule is depleted for nuclei with $A>90$. For $^{58}$Ni only 40% of the monopole sum rule is found. The excitation energy of the giant monopole resonance follows the systematic trend $\sim 80\,A^{-1/3}$ MeV. The data are also compared with folding model calculations using Tassie transition densities and an effective interaction derived from elastic data. Good agreement was obtained for low-lying quadrupole and octopole excitations, but this model yields considerably too little cross section for the monopole resonance. This probably indicates a deficiency in the Tassie model breathing mode transition density.

[NUCLEAR REACTIONS $^{208}$Pb, $^{120}$Sn, $^{90}$Zr, $^{58}$Ni, $^{46}$Ti$(\alpha,\alpha')$, $E_\alpha = 152$ MeV, $E_\chi = 0$–40 MeV; measured $\sigma(E_\chi,\theta)$; discuss giant resonances, folding model calculations, deduced $L$, $\beta_L$.]

## I. INTRODUCTION

During the past decade the existence of the giant quadrupole resonance (GQR) has been firmly established and properties of this resonance have been measured for a great many stable nuclei.[1] Of special interest are the recent direct observations[2-6] of a giant monopole resonance (GMR). The GMR is of particular importance since the energy of the resonance yields a direct measure of the nuclear incompressibility. While previous $(\alpha,\alpha')$ measurements of the GMR dealt with nuclei having $A \gtrsim 90$, a recent publication[4] has reported observation in the $(p,p')$ reaction of the GMR at a systematic excitation energy of $\sim 80A^{-1/3}$ MeV for several nuclei between $A=58$ and 208.

Most measurements of giant multipole resonances have been made by inelastic scattering of protons, electrons, and alpha particles. While protons and electrons can excite both isoscalar and isovector states, inelastic alpha scattering provides only negligible cross section for isovector resonances. Thus, the $(\alpha,\alpha')$ reaction is especially useful for studies of isoscalar, electric giant resonances, which are the subject of the present work.

Previous studies[7] of the giant quadrupole resonance using inelastic scattering of 96–120 MeV alpha's have yielded important results in the giant multipole resonance field. However, the use of higher energy alpha particles provides a significant improvement over these earlier measurements in two major ways: (1) resonance cross sections are considerably larger for incident 152-MeV alpha's than for incident 100-MeV alpha's, which leads to a larger ratio of giant resonance cross section to continuum cross section, and (2) contamination of the giant resonance portion of the inelastic alpha spectrum from the kinematic processes $\alpha + n \rightarrow {}^5\mathrm{He}^* \rightarrow \alpha + n$ and $\alpha + p \rightarrow {}^5\mathrm{Li}^* \rightarrow \alpha + p$ is eliminated. The existence of the process described in (2) has been particularly troublesome to the study of giant resonances using ~100-MeV incident alpha's. It has been shown[8] that part of the continuum distribution formed by alpha particles from the breakup of $^5$He* and $^5$Li* occurs at the same location as the GQR peak in light nuclei when 100-MeV alpha's are used. For the GMR which is located at higher excitation energies than the GQR, and is generally smaller in cross section than the GQR, the contamination from $^5$He* breakup is even more serious. However, for 152-MeV incident alpha particles the peak from the $^5$He* breakup should be at least 10 MeV away from the maximum extent of the expected location of the GMR.

In the present paper we present the results of

measurements of giant multipole resonance spectra using 152-MeV incident alpha particles. We have studied several targets in the mass range of 46–208 in order to extract systematics for the GMR and GQR. The large resonance cross sections, "clean" continuum, and selectivity of isoscalar excitations have enabled us to provide strong evidence for the GMR excitation energy systematics suggested earlier from the $(p,p')$ measurements.[4]

## II. EXPERIMENTAL RESULTS

Giant resonance spectra were obtained by inelastic scattering of 152-MeV alpha particles from the Indiana University Cyclotron Facility (IUCF). Spectra were obtained from $^{208}$Pb (4.30 mg/cm$^2$), $^{120}$Sn (4.85 mg/cm$^2$), $^{90}$Zr (4.10 mg/cm$^2$), $^{58}$Ni (4.50 mg/cm$^2$), and $^{46}$Ti (4.86 mg/cm$^2$). All targets were isotopically highly enriched and self-supporting. Inelastically scattered alpha particles were detected in a silicon surface-barrier counter telescope consisting of two 2000-$\mu$m and one 5000-$\mu$m detectors. The thickness of the "$\Delta E$" detectors was sufficient to stop ~110-MeV alpha particles. Thus, the spectra covered an excitation energy range of ~40 MeV. Particle type identification was achieved by the $\Delta E \times E$ method and the complete separation of the alpha-particle spectra from neighboring $^3$He events was achieved. Further, the thickness of the $\Delta E$ detectors was sufficient to ensure that elastically scattered alpha particles that undergo reactions in the 5000-$\mu$m detector did not interfere with the giant resonance spectra. The energy resolution of the detection system was ~150 keV.

Considerable time was spent in an effort to ensure that the spectra were free from nontarget background. No slits were utilized in the IUCF beam transport system after the final magnetic bend of the beam. Targets were mounted on thin aluminum frames with a 2.5 cm diameter aperature. Measurements were made of scattering from a blank target frame which had an aperature of only 1 cm diameter. Upon proper beam tuning, essentially no events were detected from the blank frame at the smallest scattering angle used in the experiment, 5°.

Data were taken in one degree steps for giant resonances at laboratory angles between 5° and ~25°. In the angular range of ~8°–11°, the giant resonance peaks are obscured by alpha-particle scattering from hydrogen contamination in the targets. For $^{208}$Pb, data were taken at only a few angles to compare with previous measurements[2,3] of the GQR and GMR. Elastic scattering data were also taken from $^{90}$Zr on both sides of the beam in

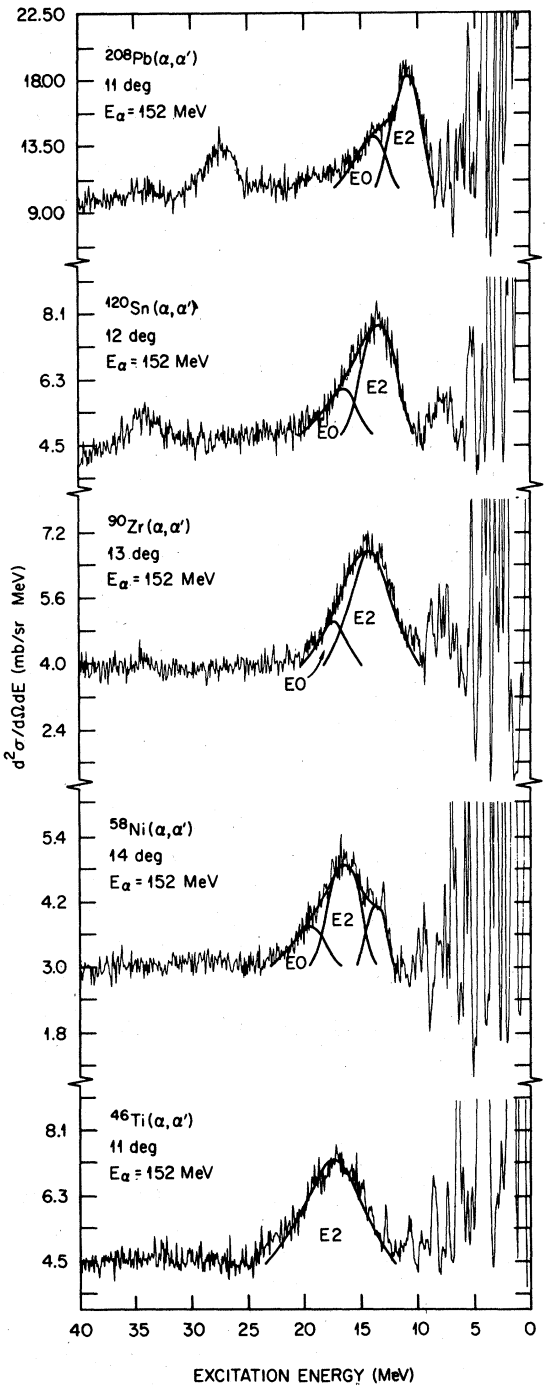


FIG. 1. Inelastic alpha-particle spectra from 152-MeV alphas incident on $^{208}$Pb, $^{120}$Sn, $^{90}$Zr, $^{58}$Ni, and $^{46}$Ti. The giant resonance structure located near the excitation energy $63A^{-1/3}$ MeV has been decomposed as shown by the solid curves in the spectra. Peaks arising from alpha scattering from hydrogen contamination on the targets are labeled ($H$). The peak cross sections for low-lying states are generally considerably off scale. The elastic scattering peak for $^{46}$Ti was experimentally suppressed.

order to determine the absolute zero angle.

Figure 1 shows spectra from five targets for scattering angles indicated on the drawing. Each of the spectra are characterized by a flat, featureless continuum which merges into the giant resonance peaks. The peak located near 27 MeV of excitation for Pb and Sn arises from alpha-particle scattering from hydrogen in the targets. It is to be noted that for the favorable angles shown on Fig. 1, the giant resonance peak rises to a magnitude nearly equal to the magnitude of the continuum. This clearly demonstrates one of the advantages discussed earlier of the use of 150-MeV alpha's.

For Sn, Zr, and Ni, the structure observed at excitation energies just below the GQR peak is from excitation of the so called low-energy octopole resonance.[9] This resonance is, in fact, comprised of $1\hbar\omega$, $3^-$ strength. For Ti, Ni, and Zr no structure is observed in the continuum at excitation energies above the GQR-GMR peak (other than the hydrogen peak). In the $^{208}$Pb and $^{120}$Sn data there is some evidence for the existence of a broad structure (several MeV wide) centered around excitation energies of 17 and 20 MeV, respectively. However, whether, and if so, to what extent, this additional structure is present depends critically on the shape assumed for the underlying continuum. However, as pointed out earlier, alpha particles from the $^5$He* breakup are certainly present in the spectra and may obscure resonance peaks, or artificially create peaks, at excitation energies higher than that of the GQR-GMR peaks. Figure 2 shows spectra at several angles from $^{120}$Sn. The enhancement of the giant resonance peak above the underlying nuclear continuum is seen to vary rapidly with angle, as is more clearly seen in the angular distributions which follow. We find that, unlike the giant resonance angular distributions, the cross section for the underlying continuum falls steadily with increasing angle over the angular range studied.

As is rather clearly seen in Fig. 1, the giant resonance peak in $^{208}$Pb is comprised of two peaks located at 10.9 and 13.9 MeV. These two peaks have been observed previously,[2,3] although somewhat less clearly, with lower energy incident alpha's and have been identified as arising from the GQR and GMR excitations. For the other nuclei we find, as was found earlier in inelastic proton scattering,[4] that the giant resonance peak is asymmetrical, being wider on the high-excitation energy side. We interpret this asymmetry as an indication of the existence of a second, weaker resonance located 2–3 MeV higher in excitation energy than the GQR. The fact that the two peaks are not well separated in the lighter nuclei as they

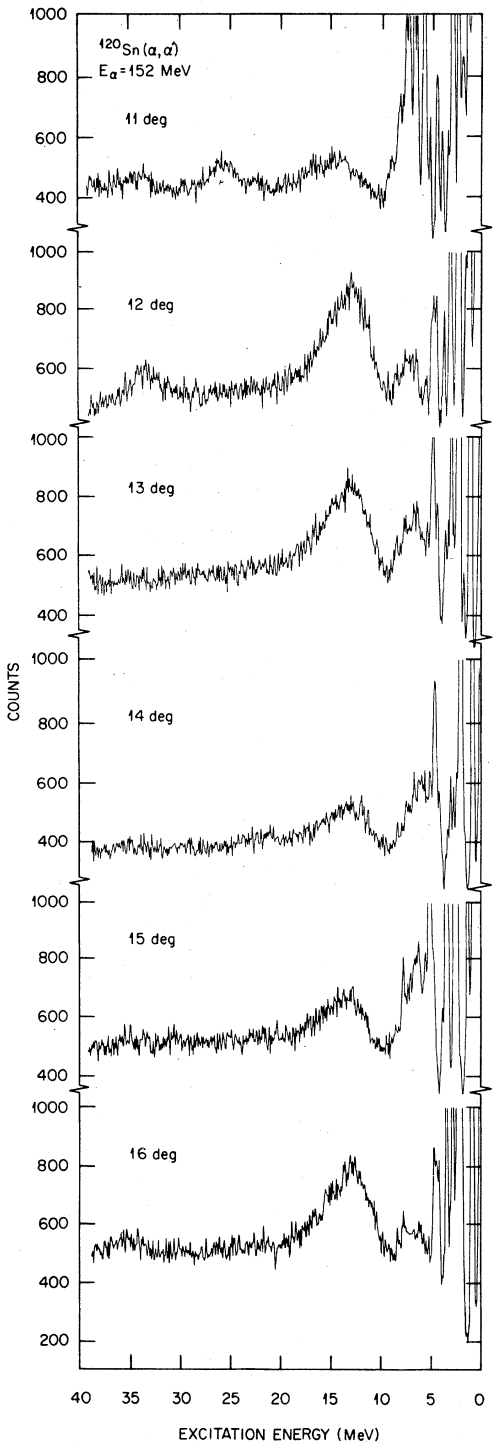


FIG. 2. Inelastic alpha-particle spectra at several angles from $^{120}$Sn bombarded by 152-MeV alpha particles. The peak located at ~13.3 MeV arises from excitation of the giant quadrupole and monopole resonances. Peaks (11°, 12°) near 30 MeV arise from alpha scattering from hydrogen contamination on the target.

are in $^{208}$Pb probably stems from the fact that the resonance widths are narrowest for nuclei in the lead region. We find no evidence for an asymmetric peak shape in $^{46}$Ti in agreement with the $(p,p')$ reaction[4] and $(\alpha,\alpha')$ reaction[10] on $^{40}$Ca.

Drawn on Fig. 1 are curves which show the shape and magnitude assumed for the nuclear continuum underlying the giant resonances and the positions and shapes we have deduced for the giant resonances. For $^{208}$Pb, $^{120}$Sn, and $^{90}$Zr we have assumed the overall resonance structure to be composed of two Gaussian shaped peaks. The location of the larger and lower excitation energy peak is $\sim 63A^{-1/3}$ MeV, while the higher excitation energy peak is found to lie at an energy of $\sim 80\,A^{-1/3}$ MeV. The extracted peak parameters are listed in Table I. The positions and width of the GQR and GMR in $^{208}$Pb agree with those extracted in previous $(\alpha,\alpha')$ measurements.[2,3] Results for $^{120}$Sn, $^{90}$Zr, and $^{58}$Ni are in agreement with results of the $(p,p')$ (Ref. 4) and $(^3\mathrm{He},^3\mathrm{He}')$ (Ref. 5) measurements.

For $^{58}$Ni the analysis of the giant resonance peak structure is considerably more complex. It is well known that an as yet not completely characterized resonance is located at ~13.5 MeV in all $fp$-shell nuclei.[1] As described in Ref. 1, the multipolarity of this resonance has been most often reported as $L=2$. However, some results strongly suggest an $L=3$ assignment. Since the 13.6-MeV resonance occurs near the neutron separation energy, the underlying continuum shape is steeply sloped and thus leads to a highly uncertain extraction of the cross section for this resonance. Our present data tend to support the $L=2$ assignment rather than the $L=3$ suggestion. However, we caution that this assignment is very uncertain. The position and shape of this resonance was assumed from earlier measurements and is indicated in Fig. 1. The remaining resonance structure (excluding the 13.6-MeV peak) is clearly asymmetrical and was analyzed in the same manner as for the heavier nuclei. For $^{46}$Ti we find no evidence for asymmetry in the shape of the giant resonance structure centered at ~18 MeV. Indeed, the $^{46}$Ti resonance is very well fitted using a single Gaussian, while the fit to the resonance structure (as determined by minimum $\chi^2$ in a Gaussian peak fitting routine) in all heavier nuclei we have studied requires the use of two Gaussians. We have, therefore, treated the

TABLE I. Parameters of the GQR and GMR peaks deduced from 152-MeV alpha particle inelastic scattering.

| Nucleus | | Excitation energy (MeV) | Width (MeV) |
|---|---|---|---|
| $^{46}$Ti | GQR | 17.6±0.3 | 6.6±0.4 |
| $^{58}$Ni | GQR | 16.0±0.5 | 3.6±0.4 |
| | GMR | 20.0±0.5 | 3.0±0.5 |
| $^{90}$Zr | GQR | 14.1±0.5 | 3.6±0.5 |
| | GMR | 17.5±0.5 | 2.9±0.5 |
| $^{120}$Sn | GQR | 13.3±0.3 | 3.7±0.5 |
| | GMR | 16.9±0.4 | 3.3±0.5 |
| $^{208}$Pb | GQR | 10.9±0.3 | 2.4±0.4 |
| | GMR | 13.9±0.4 | 3.2±0.4 |

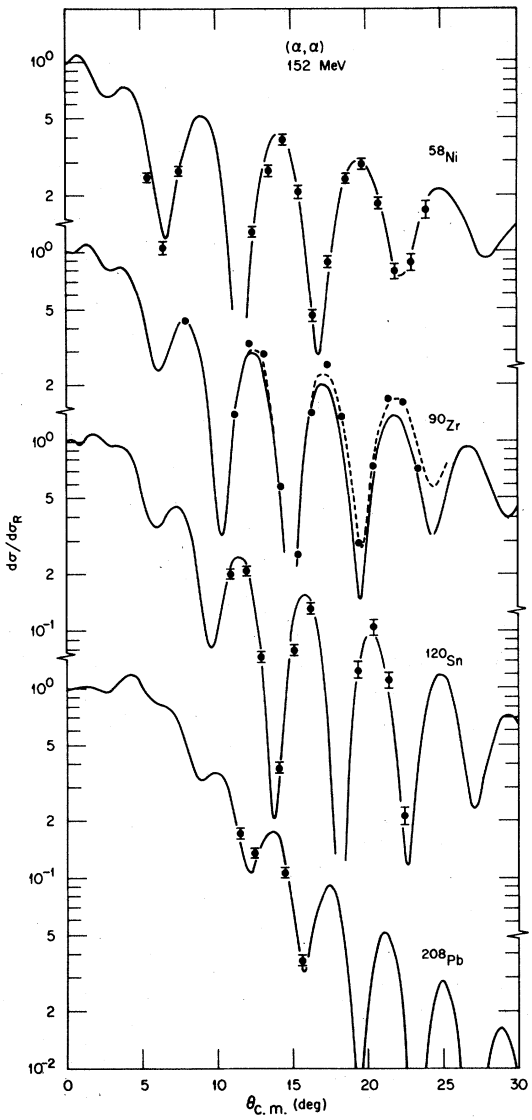


FIG. 3. Elastic scattering of 152-MeV alpha particles. The solid curves are predicted cross sections using folded potentials obtained by fitting elastic data at 140 MeV: see text and Table II. The dashed curve for $^{90}$Zr gives the predictions when the absorptive strength is reduced to 17.4 MeV, the optimum value for these 152 MeV data.

$^{46}$Ti giant resonance as a single quadrupole excitation.

Our assumption then is that the broad peak observed in all the nuclei studied other than $^{46}$Ti is composed of peaks from excitation of the GQR and GMR. Such an assumption has been verified in small angle $(\alpha,\alpha')$ and $(^3\mathrm{He},^3\mathrm{He}')$ measurements[3,5] in $^{208}$Pb, $^{144}$Sm, and $^{90}$Zr, and the same assumption has been made in an analysis of $(p,p')$ data.[4] In the present data we do not have to contend with the presence of the giant dipole resonance as is the case in the $(p,p')$ reaction. Further, as discussed above, the 152 MeV resonance cross sections are larger and the continuum is cleaner than for lower energy inelastic alpha-particle scattering.

The cross sections extracted for elastic scattering and inelastic scattering to low-lying $2^+$ and $3^-$ levels are shown in Figs. 3 and 4, respectively. The cross sections measured for the two resonance

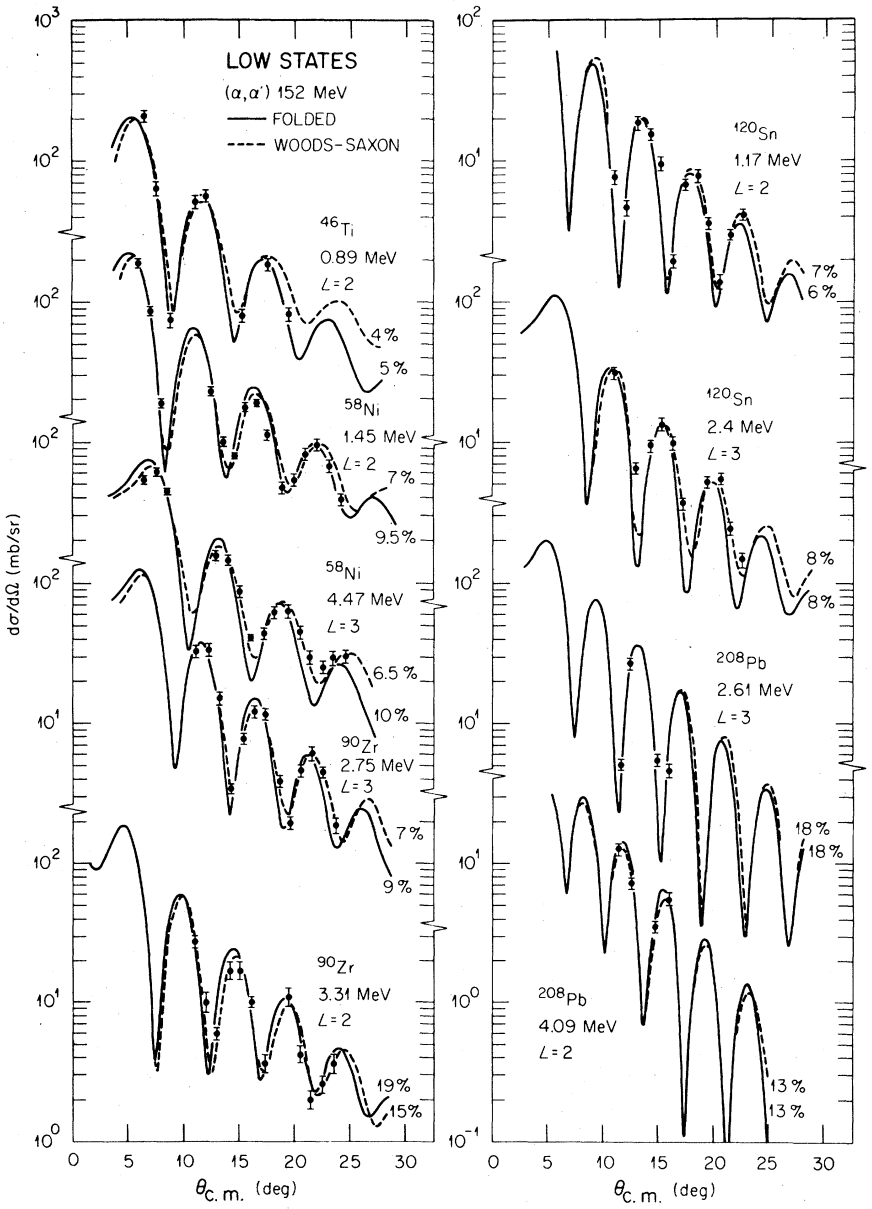


FIG. 4. Cross sections for excitation of low-lying excited states. The curves are theoretical cross sections normalized to the data by the sum rule limit percentages indicated. Solid curves: folding model; dashed curves: deformed Woods-Saxon potentials.

peaks extracted for each target nucleus (only one peak for $^{46}$Ti) are plotted in Fig. 5. The calculated curves shown in Figs. 3, 4, and 5 will be discussed in the next section. The uncertainties shown on the giant resonance cross sections are a minimum of 20%. These uncertainties are absolute and arise mainly from the uncertainty in the shape and magnitude assumed for the nuclear continuum underlying the giant resonances. The subject of the uncertain continuum extrapolation beneath the

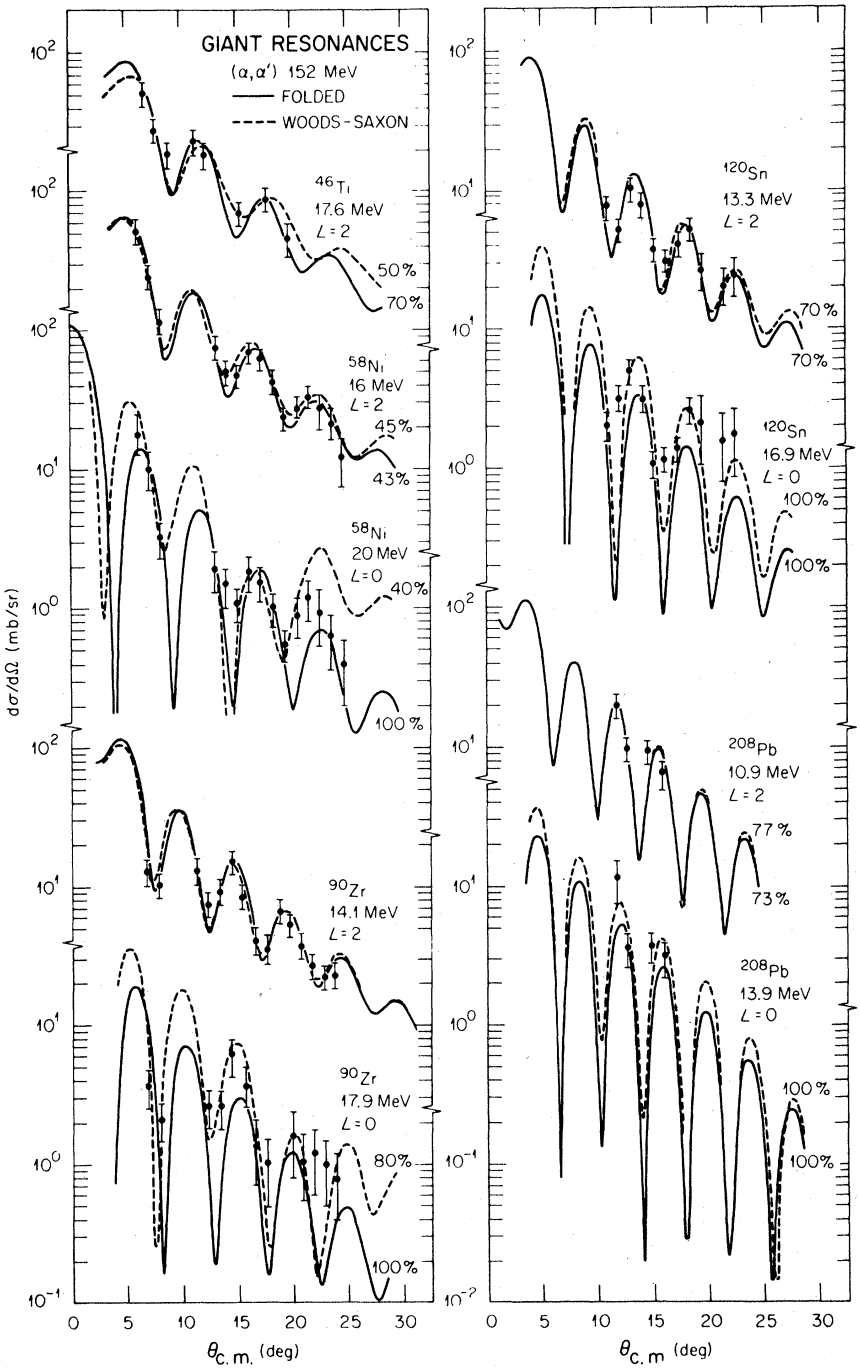


FIG. 5. Cross sections for excitation of giant resonance states. The curves are theoretical cross sections normalized to the data by the sum rule limit percentages indicated. Solid curves: folding model; dashed curves: deformed Woods-Saxon potentials.

resonance has been discussed in detail in Refs. 1 and 7 and we follow the techniques discussed therein.

## III. THEORETICAL ANALYSIS

### A. Elastic scattering and optical models

#### *1. Woods-Saxon potentials*

Our data for elastic scattering are not complete enough for a definitive optical model analysis to be made. However, rather complete elastic data have been taken elsewhere[11] at about 140 MeV for the targets $^{46}$Ti, $^{58}$Ni, $^{90}$Zr, and $^{208}$Pb. Further, $^{120}$Sn + $\alpha$ elastic scattering has been measured[12] at 166 MeV. These data were analyzed using 6-parameter Woods-Saxon potentials of the usual form

$$U(r) = -V(1+e^{x_v})^{-1} - iW(1+e^{x_w})^{-1}, \quad (1)$$

where

$$x_v = (r - R_v)/a_v, \quad x_w = (r - R_w)/a_w .$$

Here $R_v = r_v A^{1/3}$, $R_w = r_w A^{1/3}$, and $A$ is the mass number of the target. We used parameter sets from those analyses in the present work since they were found to reproduce satisfactorily our elastic data at 152 MeV. The parameter values are listed in Table II. In each case the Coulomb potential from a uniformly charged sphere of radius $1.3A^{1/3}$ fm was added to the nuclear potential of Eq. (1).

#### *2. Folded potentials*

Because of our intention to apply the folding model to the inelastic scattering measurements, the elastic data[11] at 140 MeV were also analyzed using this approach in order to determine the effective interaction parameters. The folding model used is the standard one[13] and consists of a nucleon-alpha interaction $v_{N\alpha}$ folded into the density distribution $\rho(r)$ of the target nucleus:

$$U_F(r) = \int \rho(r') v_{N\alpha}(|r - r'|) dr' . \quad (2)$$

The construction of densities for use in folding calculations has been discussed elsewhere.[14] The densities of Negele[15] were used for $^{40}$Ca, $^{90}$Zr, and $^{208}$Pb, while the shell model was used[14] to construct densities for the other targets. That for $^{58}$Ni was as described in Ref. 14, except that the neutron well depth was increased to 60 MeV; this reduces the neutron rms radius to 3.64 fm so that it is 0.08 fm smaller than the proton radius, in better agreement with recent analyses of 1 GeV proton scattering.[16] We assumed that the least-bound neutrons and protons in $^{46}$Ti were purely $1f_{7/2}$ with binding energies given by the separation energies. The shell model potential used was similar to that adopted[14] for $^{58}$Ni except both neutron and proton wells were taken to be 55 MeV deep. This gave rms radii of 3.493 fm (protons) and 3.475 fm (neutrons). The protons in $^{120}$Sn were assumed to occupy the $Z = 50$ closed shells, while the configuration $(1g_{7/2})^8(1h_{11/2})^6(2d_{5/2})^6$ was adopted for the neutron excess. Again, shell model potentials with the same geometry were used, but with depths of 50 MeV (protons) and 60 MeV (neutrons). These result in rms radii of 4.581 fm (protons) and 4.807 fm (neutrons), which seem to be in reasonable agreement with electron and high-energy proton scattering data.[16]

We also need to specify the effective interaction $v_{N\alpha}$. In the present work we are concerned with inelastic data for quite small scattering angles, $\theta \lesssim 25°$, In these circumstances it is quite sufficient to use a simple 3-parameter density-independent Gaussian model for $v_{N\alpha}$ with a complex strength. (Consequently, the real and imaginary parts of $U_F(r)$ have the same radial shape. This is in contrast to the Woods-Saxon potentials of Table II which have imaginary parts with radii significantly larger than the radii of their real parts. However, these latter potentials were obtained[11] by fitting data out to much larger angles, beyond the rainbow angle.) Then our interaction is

$$v_{N\alpha}(s) = -(V_F + iW_F)e^{-(r/\alpha)^2} . \quad (3)$$

The parameters $V_F$, $W_F$, and $\alpha$ were determined by fitting at small angles ($\theta \leq \theta_{max}$) the 140 MeV elastic data[11] for $^{40}$Ca, $^{58}$Ni, $^{90}$Zi, and $^{208}$Pb. The values of $V_F$ and $W_F$ were optimized, using the standard $\chi^2$ criterion, for a series of values of the range $\alpha$. The results given in Fig. 6 show that there are well-defined minima in $\chi^2$ for essentially the same value of $\alpha$ for each target. We use here the average value $\alpha = 1.94$ fm, which is very close to the value 1.95 fm adopted by the Karlsruhe group[17] and similar to the long popular[12,13,18] $\alpha = 2$ fm. With this choice we are reduced to a 2-parameter model. The corresponding optimum values of $V_F$ and $W_F$ are given in Table III. These are in good agreement with those found previously[13,17,18] with this model. The average

TABLE II. Woods-Saxon optical model parameters.

| Target | $V$ (MeV) | $r_v$ (fm) | $a_v$ (fm) | $W$ (MeV) | $r_w$ (fm) | $a_w$ (fm) |
|---|---|---|---|---|---|---|
| $^{46}$Ti | 118.2 | 1.24 | 0.79 | 20.47 | 1.59 | 0.57 |
| $^{58}$Ni | 118.2 | 1.24 | 0.79 | 20.47 | 1.59 | 0.57 |
| $^{90}$Zr | 117.5 | 1.27 | 0.78 | 21.02 | 1.56 | 0.57 |
| $^{120}$Sn | 119.4 | 1.26 | 0.76 | 30.7 | 1.43 | 0.70 |
| $^{208}$Pb | 110 | 1.32 | 0.71 | 21.3 | 1.51 | 0.67 |

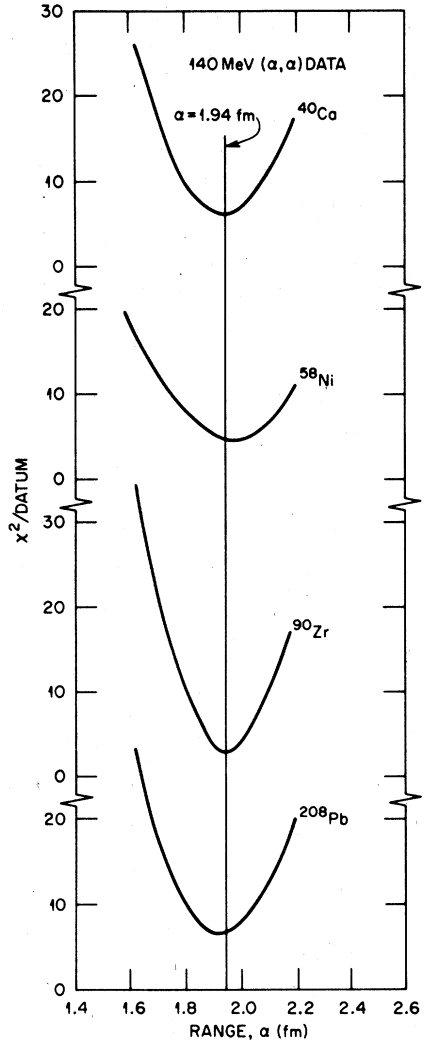


FIG. 6. Variation of $\chi^2$ with the range of the Gaussian $v_{N\alpha}$ used in the folding model when the real and imaginary strengths are optimized to fit elastic data at forward angles (see Table II) for 140-MeV alpha particles. The quoted experimental errors were used.

volume integral per nucleon of $v_{N\alpha}$ has the value $(370+229i)$ MeV fm$^3$.

For reference we also give in Table III the strong absorption radii $R_{SA}$, defined as the distance of closest approach for the Rutherford orbit, which has the same angular momentum $L_{1/2}$ as that for which the optical model indicates a transmission coefficient $T_{L_{1/2}}=\frac{1}{2}$. It is well known[13] that the forward scattering (elastic and inelastic) is most sensitive to the interaction potential in the region $r \simeq R_{SA}$. (The values of $R_{SA}$ at 152 MeV are very close to those at 139 MeV.)

It was verified that these folding model parameters also gave satisfactory agreement at 152 MeV with the elastic data taken in the present experiment for the same targets. The curves shown in Fig. 3 correspond to the folding parameters determined from the 140 MeV data, except for $^{120}$Sn. In this case the 152 MeV data themselves were used to obtain the $V_F$ and $W_F$ given in Table III. The 152 MeV data for the target $^{90}$Zr show some tendency to decrease less rapidly with increasing angle than the predictions. The dashed curve in Fig. 3 shows the improvement obtained by reducing $W_F$ from 21.1 MeV (Table III) to 17.4 MeV. This is 23% smaller than the average value from Table III, but fortunately this ambiguity only leads to some 10% uncertainty in the cross sections predicted for the inelastic scattering.

### B. Inelastic scattering models

The data obtained for inelastic scattering were analyzed using the distorted-wave Born approximation (DWBA). Two models were used for the transition potentials.[19] The distorted waves were generated from the corresponding optical potentials (Table II or III). We extract the percentage depletion of the standard energy-weighted sum rules (EWSR)[19] by comparison with the measured cross sections.

TABLE III. Folding model potential parameters for $\alpha = 1.94$ fm.

| Target[a] | $\alpha_{max}$ | $V_F$ (MeV) | $W_F$ (MeV) | $L_{1/2}$ | $R_{SA}$ (fm) | $-\mathrm{Re}U_F(R_{SA})$ (MeV) | $\langle r^2\rangle^b$ (fm$^2$) |
|---|---|---|---|---|---|---|---|
| $^{40}$Ca | 27° | 37.4 | 21.5 | 30.5 | 6.8 | 4.4 | 11.46 |
| $^{46}$Ti | 25° | 36.7 | 24.3 | 31.9 | 7.1 | 3.9 | 12.13 |
| $^{58}$Ni | 30° | 35.5 | 21.5 | 33.4 | 7.3 | 4.0 | 13.55 |
| $^{90}$Zr | 30° | 36.4 | 21.1 | 38.3 | 8.2 | 3.9 | 18.02 |
| $^{120}$Sn | 23° | 31.9 | 20.4 | 42.8 | 8.8 | 3.6 | 22.22 |
| $^{208}$Pb | 46° | 40.5 | 26.0 | 47.4 | 10.4 | 3.0 | 31.42 |
| Average | | 36.4±2.5 | 22.5±2.0 | | | | |

[a] Data (Ref. 11) at 140 MeV for $\theta \leq \theta_{max}$ fitted, except for $^{120}$Sn, where the results are for fits to 152 MeV data taken in the present work.

[b] Mean square radius of the ground-state density distribution used in the folding calculation.

*1. Deformed Woods-Saxon potential model*

This is the standard model in which the surface $r=R$ of the Woods-Saxon optical potential (1) is deformed. The resulting transition potentials for isoscalar, normal-parity excitations with $L \geq 2$ have the radial form[19]

$$U_{tr}(r) = \beta_L R\, dU(r)/dr, \quad L \geq 2 \tag{4}$$

where $\beta_L$ is the deformation parameter to be determined by comparison with the data. In the case of the potential (1), the prescription (4) is applied separately to the real and imaginary parts; we assumed the same value of $\beta_L$ for both parts. A similar expression,[19] supplemented by a volume-conserving term, was used for the isoscalar breathing mode with $L=0$:

$$U_{tr}(r) = \alpha[3U(r) + r\, dU(r)/dr], \quad L=0. \tag{5}$$

In this model the usual isoscalar EWSR for $L \geq 2$ may be expressed as

$$S_L = \sum_i E_i \beta_L^2(i) = (\hbar^2/2m\langle r^2\rangle)(4\pi/5A)L(2L+1), \tag{6}$$

where $\beta_L(i)$ is the deformation parameter for exciting the $i$th excited state whose excitation energy is $E_i$. Also, $m$ is the nucleon mass and $\langle r^2\rangle$ is the mean square radius of the ground-state density distribution (see Table III). For isoscalar monopole excitations we have instead

$$S_0 = \sum_i E_i \alpha^2(i) = \hbar^2/2m\langle r^2\rangle A. \tag{7}$$

Although these sum rules are only approximate, they provide a useful standard by which to measure the strengths of giant resonance excitations.

*2. Folding model transition potentials*

In this approach[14] the transition density (in general, nonspherical) is inserted into the folding integral (2) in order to give the transition potential. The transition density may be obtained from microscopic structure calculations, for example,[20] those using the random-phase approximation (RPA). In principle, these calculations provide the magnitude as well as the shape of the density (unless one is using the analog to an "effective charge" to compensate for truncation of the model space used). However, there are a number of uncertainties whose importance has not been determined. Most calculations of this type result in discrete energy levels even for the unbound states such as the giant resonances. If the RPA is used, these states are simply composed of 1-particle, 1-hole configurations (with some ground-state correlation effects built in, of course). In practice, the unbound states will be broadened by particle emission. They also couple to the background of 2-particle, 2-hole states which causes them to be spread and mixed. These points are of importance because it is the tails of the transition densities which contribute most to the folding integral for the potential near the strong absorption radius. In the case of $\alpha + {}^{208}$Pb, for which $R_{SA} \simeq 10.4$ fm, calculations for the $3^-$ first excited state indicate that the transition density needs to be known accurately out to $r=12$ fm or more in order to give the transition potential accurately at $R_{SA}$. A density which is cut off at $r=10.4$ fm results in an error of about 10% in $U_{tr}(R_{SA})$, or about 20% in cross section. Most RPA calculations do not provide densities which are accurate out to such large radii, not because they cannot, but because they are not needed for other purposes and it would be computationally expensive to do so.

Finally, such calculations are only available for a limited number of nuclei. Consequently we felt it was worth using a simplified model for the transition densities. If the EWSR of Eq. (6) is exhausted by excitation of a single state, it has been shown[21] that the corresponding transition density is the same as that given by the Tassie or hydrodynamical model whose radial part has the form

$$\rho_{tr}(r) = \alpha_L r^{L-1} d\rho(r)/dr, \quad L \geq 2 \tag{8}$$

where $\rho(r)$ is the ground state density distribution. The corresponding result for the $L=0$ compressional mode is

$$\rho_{tr}(r) = \alpha_0[3\rho(r) + r\, d\rho(r)/dr], \quad L=0. \tag{9}$$

If the excitation energy of the state is $E$, the amplitudes are given by

$$\alpha_L^2 = \left(\frac{\hbar^2}{2m}\right)\frac{4\pi L}{EA\langle r^{2L-2}\rangle}, \quad \alpha_0^2 = \left(\frac{\hbar^2}{2m}\right)\frac{1}{EA\langle r^2\rangle}, \tag{10}$$

where again the averages $\langle r^n\rangle$ are to be taken over the ground-state density distribution. The "doorway dominance" hypothesis of Fallieros *et al.*[21] then suggests that the transition densities of Eqs. (8) and (9) are a good approximation for those strong transitions which exhaust a large fraction of the isoscalar sum-rule strength. In the present study we also used them for transitions to the low-lying states, even though these carry a much smaller fraction of the EWSR. The ground-state densities $\rho(r)$ used in Eqs. (8) and (9) were the same as those employed in the calculations of the folded optical potentials.

The remarks made above about the sensitivity of the results to the tail of the trasition density apply here also, of course. The main advantage

of this hypothesis is one of simplicity and "reasonableness"; it also provides an unambiguous prescription for the tails of the densities. Further, these Tassie forms are frequently used for charge densities in analyses of inelastic electron scattering; in principle, we then have a consistent way of comparing results from electron and hadron measurements. Previous comparisons have been somewhat ambiguous because, while analyses of electron measurements often use Tassie densities, the deformed potential models (4) and (5) have been used to extract strengths from hadronic scattering. The precise relationship between these quantities is not clear.

Figure 7 provides two examples of comparisons of transition potentials from the folding and from the deformed potential. Only the real parts are shown. The overall shapes obtained from the two models are significantly different. [These differences are even more marked for the imaginary parts, for while our folding model gives both parts with the same shape, the imaginary part of the deformed Woods-Saxon potential peaks at even larger radii, at $r = 8.94$ fm for $^{208}$Pb (see Table II). However, when comparing the imaginary shapes we must remember that the folded potential was obtained by fitting elastic data at small angles, but the Woods-Saxon potential was required to fit the large angle data also.] However, the two models give much more similar results in the important region near the strong absorption radius, $r \simeq R_{SA}$. The real folded potential is slightly (~10%) larger at $r = R_{SA}$, but the imaginary part is slightly smaller (~20%) than the deformed Woods-Saxon for the shape oscillations ($L \geq 2$). Consequently, both models give similar cross sections for these transitions. The monopole $L = 0$ behaves quite differently; both parts of the folded potential are smaller at $r = R_{SA}$, so that the folding-plus-Tassie model predicts about $\frac{2}{3}$ the cross section given by the deformed potential.

For comparison, calculations were also made for $^{208}$Pb assuming transition densities closer in spirit to the deformed potential model of Eq. (4):

$$\rho_{tr}(r) = \beta_L R_\rho d\rho(r)/dr, \quad L \geq 2 \tag{11}$$

where $R_\rho$ is the radius where $\rho(r)$ falls to half its central value. The density (11) peaks at a slightly smaller radius than the Tassie density (8) because of the absence of the $r^{L-1}$ factor. Further, alpha scattering weights the large radii even more than $r^{L-1}$ so that, for a given depletion of the EWSR, the cross section predicted by use of Eq. (11) is somewhat smaller than predicted for the Tassie density. The reduction in cross section for $^{208}$Pb is about 20% for $L = 2$ and 33% for $L = 3$. We shall see below that for excitation of the 2.61 MeV $3^-$ level in $^{208}$Pb the use of the Tassie density gives excellent agreement with measured $B(E3)$ values whereas use of the density (11) does not. The shapes of the predicted angular distributions, however, are almost indistinguishable.

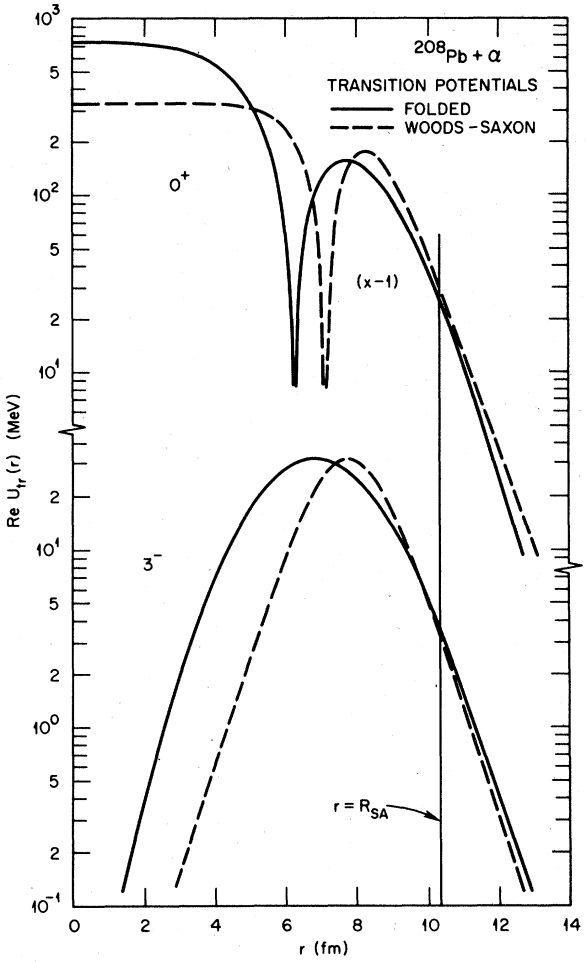


FIG. 7. Real parts of the transition potentials for excitation of $3^-$ and breathing mode $0^+$ states in $^{208}$Pb by alpha-particle scattering. Solid curves: folding model, using Tassie transition densities; dashed curves: deformed Woods-Saxon potential. The strong absorption radius $r = R_{SA}$ for alpha's of 140 MeV is indicated. The monopole density is normalized to unit amplitude ($\alpha = 1$), while the octupole density corresponds to 18% of the EWSR.

### 3. *Electric transition rates*

Transition strengths are frequency expressed in terms of $B(EL)$ values. If the proton transition density is $\rho^p_{tr}(r)$, we normalize it so that

$$B(EL)\uparrow = \left| \int \rho^p_{tr}(r) r^{L+2} dr \right|^2 e^2, \quad L \geq 2. \tag{12}$$

It is in the spirit of the collective model for strong

isoscalar transitions to assume[18] that the proton part is related to the total transition density by

$$\rho_{tr}^{p}(r) = (Z/A)\rho_{tr}(r). \quad (13)$$

It is easy to verify that the transition density (8) with the amplitude (10) exhausts the EWSR with

$$B(EL)\uparrow \left(\frac{\hbar^2}{8\pi m}\right)\left(\frac{Z}{A}\right)^2 \frac{AL(2L+1)^2\langle r^{2L-2}\rangle}{E} e^2. \quad (14)$$

For monopole $E0$ transitions it is common to use the definition

$$B(E0) = \left|\int \rho_{tr}^{p}(r) r^4 dr\right|^2 e^2. \quad (15)$$

Making the same assumption (13) for isoscalar excitions, the density (9) with amplitude (10) also exhausts the EWSR with

$$B(E0) = \left(\frac{2\hbar^2}{m}\right)\left(\frac{Z}{A}\right)^2 \frac{A\langle r^2\rangle}{E} e^2. \quad (16)$$

It is possible to calculate the proton and neutron parts of $\rho_{tr}(r)$ separately with the independent-particle model we use for the ground state density $\rho(r)$. This was done for a few cases. Although significant deviations from the *ansatz* (13) are found as a function of $r$, it gives the averages $\langle r^n\rangle$ correctly to within a few percent.

### C. Applications to inelastic data

The curves in Figs. 4 and 5 are fits to the present data using the models just described; the solid curves are from the folding model and the dashed curves are from the deformed potential model. Also indicated are the percentages of the EWSR deduced from Eqs. (6), (7), and (10). These results are collected in Table IV for the low-lying states and Table V for the giant resonances. The GMR curves for the folding model in Fig. 5 are drawn for 100% of the EWSR, while Table V gives percent estimates to fit the data. In some cases there is uncertainty as to the best way to normalize the theoretical curves to the data. However, the strength required for choices other than those shown in the figures are easily obtained by scaling the values shown.

Except in the case of $^{208}$Pb, Coulomb excitation contributions were not included in the calculations. Even for $^{208}$Pb the cross section magnitudes were changed only a few percent by inclusion of Coulomb excitation with very slight angular distribution changes in the angular regions shown.

#### *1. The 2.61 MeV 3⁻ state of $^{208}$Pb*

This transition is particularly useful for studying the validity of the models. It is strong, has been studied intensively by inelastic electron scattering,[23] and the $B(E3)$ value is well known. Further, various RPA structure calculations[20] indicate a theoretical transition density which is quite similar to the Tassie transition density of Eq. (8). Although the present data for this state (Fig. 4) are very sparse, extensive data were obtained[11]

TABLE IV. Results for low excited states as percentages of the EWSR.

| Target | $E$ (MeV) | Folded[a] potential | Deformed[a] potential | $B(EL)$ (% EWSR) | % EWSR from other $(\alpha,\alpha')$ data[b] |
|---|---|---|---|---|---|
| $2^+$ states | | | | | |
| $^{46}$Ti | 0.889 | 5 | 4.0 | 7.8±0.3 | |
| $^{58}$Ni | 1.454 | 9.5 | 7 | 6.7±0.2 | 7.5[c] |
| $^{90}$Zr | 3.309 | 19[g] | 15 | | 7[d] |
| $^{120}$Sn | 1.17 | 6 | 7 | 5.3±0.1 | |
| $^{208}$Pb | 4.086 | 13 | 13 | 13.0±1.3 | |
| $3^-$ states | | | | | |
| $^{58}$Ni | 4.47 | 10 | 6.5 | 10 | 7.5[c] |
| $^{90}$Zr | 2.748 | 9[h] | 7 | 5.8±0.2 | 15±5[e] |
| $^{120}$Sn | 2.4 | 8 | 8 | 8 | |
| $^{208}$Pb | 1.615 | 18 | 18 | 17.5±1.0 | 18[c,e] |
| | | | | | 20[f] |

[a] Values quoted are those used for the curves in Fig. 3.
[b] Reanalyzed using the same folded potential as used to analyze present data.
[c] From $(\alpha,\alpha')$ data (Ref. 11) at 140 MeV.
[d] From $(\alpha,\alpha')$ data (Ref. 22) at 115 MeV.
[e] From $(\alpha,\alpha')$ data (Ref. 22) at 96 MeV.
[f] From $(\alpha,\alpha')$ data (Ref. 2) at 120 MeV.
[g] Reduced to about 16% if $W_F$ = 17.4 MeV used.
[h] Reduced to about 8% if $W_F$ = 17.4 MeV used.

TABLE V. EWSR depletion for giant resonances.

| Target | $E_x$ (MeV) | % EWSR[a] folded potential | % EWSR[a] deformed potential | % EWSR[b] $(e, e')$ | % EWSR[c] other $(\alpha, \alpha')$ |
|---|---|---|---|---|---|
| | | | Isoscalar quadrupole | | |
| $^{46}$Ti | 17.6 | 70 ± 14 | 50 ± 10 | | |
| $^{58}$Ni | 16.0 | 43 ± 10 | 45 ± 10 | 57 ± 6<br>48 ± 6 | 43[d] |
| $^{90}$Zr | 14.1 | 75[e] ± 15 | 65 ± 13 | 56 ± 17 | ~50[f] |
| $^{120}$Sn | 13.3 | 70 ± 15 | 70 ± 15 | | |
| $^{208}$Pb | 10.9 | 73 ± 15 | 77 ± 15 | 95 ± 35 | 80[f]<br>~75[g] |
| | | | Isoscalar monopole | | |
| $^{46}$Ti | | Not observed | | | |
| $^{58}$Ni | 20.0 | 120 ± 20 | 40 ± 10 | | |
| $^{90}$Zr | 17.0 | 180[e] ± 40 | 80 ± 20 | | |
| $^{120}$Sn | 16.9 | 150 ± 20 | 100 ± 20 | | |
| $^{208}$Pb | 13.9 | 140 ± 30 | 100 ± 20 | | 105 ± 20[h]<br>125 ± 25[g]<br>85[i] |

[a] Values quoted for the GQR are those used for the curves in Fig. 5.
[b] From Ref. 1.
[c] Reanalyzed using the same folded potential as used to analyze the present data.
[d] From 115-MeV $(\alpha, \alpha')$ data of Ref. 22.
[e] Reduced by ~15% if $W_F$ = 17.4 MeV is used (see Fig. 3).
[f] From 96-MeV $(\alpha, \alpha')$ data of Ref. 22.
[g] From 120-MeV $(\alpha, \alpha')$ data of Ref. 2.
[h] From data of Ref. 3 (Youngblood *et al.*).
[i] From Ref. 6 from which the authors' folding model analysis appears to be the same as that used in the present paper.

at 139 MeV and other data are available[22] at 96 MeV. These are shown in Fig. 8 together with the folding model fits. (The calculations for all three energies were made using the same parameters.)

The measured $B(E3)$ is $(6.65 \pm 0.35) \times 10^5\ e^2\,\mathrm{fm}^6$, which is $(17.5 \pm 0.9)\%$ of the EWSR (14). The theoretical curves shown in Figs. 4 and 8 for this transition also use this value. The agreement with the measured $(\alpha, \alpha')$ cross sections at all three energies is seen to be excellent. This result lends further support to the use of the Tassie density with the idea[18] of relating hadron cross sections to $B(EL)$ values through the *ansatz* of Eq. (13). On the other hand, when we use in the folding model the density of Eq. (11), normalized to correspond to the same $B(E3)$ value, the theoretical cross sections are only $\frac{2}{3}$ as large as the measured ones.

### 2. *Other low-lying excited states*

Data and calculated cross sections for several other low-lying excited states are shown in Fig. 4; the overall agreement is good. There is a tendency for the folding model cross sections to

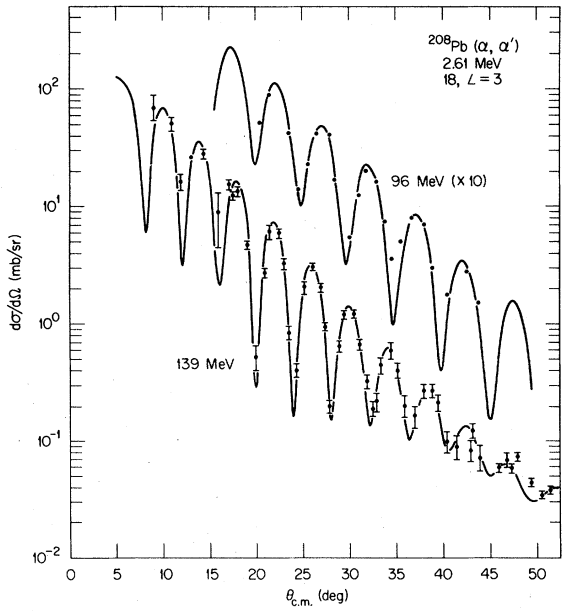


FIG. 8. Comparison of folded potential predictions, using 18% of the EWSR, with measured cross sections for the 3$^-$ state at 2.61 MeV in $^{208}$Pb.

peak at slightly smaller angles than the deformed potential ones. Both models yield similar depletions of the EWSR, within the uncertainties of fitting to the data, although there is a tendency for the folding model to require more strength for the lighter targets.

In the case of the 1.45-MeV $2^+$ state in $^{58}$Ni, the measured[24] $B(E2) = 695 \pm 20\ e^2\,\mathrm{fm}^4$ represents $(6.7 \pm 0.2)\%$ of the EWSR. This is in good agreement with the deformed potential fit for this state, while the folding model requires about 1.4 times this amount. There is an even bigger difference for exciting the 4.47-MeV $3^-$ state, although here it is the folding model which is in agreement with the measured[18] $B(E3)$ value of $(10.1 \pm 0.3)\%$ of the EWSR. Excitation of these levels in $^{58}$Ni by $(\alpha, \alpha')$ has also been studied[11] with 139 MeV incident alphas. A fit to those data with the present folding model depletes about 7.5% ($2^+$) and 8% ($3^-$) of the EWSR. Data for the $2^+$ level taken[22] with 115-MeV alpha's, although less complete, are in agreement with calculations using the 6.7% deduced from the $B(E2)$ value. Hence there are some uncertainties associated with these two transitions.

Both models yield sum rule depletions for $^{46}$Ti which are not much more than one half of the $(7.8 \pm 0.3)\%$ deduced from the $B(E2)$ value.[24] On the other hand, the measured $B(E3)$ for the 3.31-MeV state of $^{90}$Zr and the $B(E2)$ for the 1.17-MeV state of $^{120}$Sn indicate somewhat smaller fractions of the EWSR than are obtained from the present measurements. It is not clear whether these discrepancies represent failures of the models for these transitions or merely (as may be the case for $^{58}$Ni) uncertainties in the various measurements. The fits to the data for the 2.4-MeV $3^-$ state in $^{120}$Sn and the 4.09-MeV $2^+$ state in $^{208}$Pb are in perfect agreement with the $B(E2)$ measurements.

Use of the folded potential adjusted to fit the 152-MeV elastic data for $^{90}$Zr ($W_F = 17.4$ MeV, dashed curve in Fig. 3) merely increases the calculated cross sections by about 10% and hence reduces the deduced sum rule percentages by the same fraction.

### D. The giant resonances

The giant resonance results are shown in Fig. 5. The two models yield essentially the same sum rule depletion percentages for the giant quadrupole $L = 2$ resonances, except for $^{46}$Ti, where the folding approach yields about 1.4 times as much depletion as the deformed potential model. The angular distributions are in good agreement for both models. The transition strengths deduced are summarized in Table V.

The situation is quite different for excitation of the giant monopole, $L = 0$, $T = 0$, resonances. Although both modes give acceptable angular distributions, the folded potential consistently predicts a much smaller cross section than the deformed potential of Eq. (5). Indeed, its predictions are smaller than the measured cross sections for $^{90}$Zr and heavier targets even with 100% of the sum rule limit. This discrepancy persists to the same degree when comparisons are made with data at other energies. The difference between the folding model and the deformed potential model in this case can be understood from Fig. 7, which shows that the folding model yields an appreciably weaker interaction in the important region near the strong absorption radius.

There can be contributions to the cross section in this excitation region from the isovector giant dipole resonance which almost coincides with the giant monopole. These can arise from Coulomb excitation, and also by nuclear interaction when the neutron and proton transition densities have different shapes,[25] even though the alpha is an isoscalar particle. However, calculations for $^{208}$Pb indicate that these effects, while not completely negligible, do not significantly affect the comparison we have made with the data. The main effect is to fill in the deep minima associated with the pure monopole excitation and to increase the peak cross sections by no more than ~10%.

The monopole part of the interaction $v_{N\alpha}$ is just that part which determines the elastic optical potential and this was used to determine the parameters of $v_{N\alpha}$. Further, its use for higher multipoles seems to be reasonably successful, especially for $^{208}$Pb. However, there may be some uncertainty associated with the imaginary part of $v_{N\alpha}$; it is not obvious that the couplings to other channels that this part represents will manifest themselves in exactly the way that our simple folding model predicts. The breathing mode excitation may be particularly sensitive to this because of the difference of two terms that appears in Eq. (9). In the present calculations for $^{208}$Pb, for example, the imaginary part of the interaction is responsible for 30% of the $0^+$ cross section of the folding model, or 40% of that from the deformed potential model. Otherwise we must conclude that the Tassie model [Eq. (9)] is not quite correct for the transition densities for these monopole excitations. The Tassie density used here for $^{208}$Pb appears to be close to that obtained[26] from RPA calculations and, indeed, the calculated (Wambach *et al.*[20]) cross sections using the RPA density for excitation of the $0^+$ state by $(p, p')$ appear to be only about one half those observed[4] with 60-MeV protons. The calculated $2^+$ cross sections, on the other hand, are in agreement with the mea-

surements. Similar results were obtained in the earlier calculations of Halbert *et al.*[20] For example, a value of 2.6 mb/sr for the peak at 13.5° was predicted for 115-MeV $(\alpha,\alpha')$ excitation of the giant monopole resonance while the observed[2] value at 120 MeV is about 4.5 mb. (The present model predicts 2.9 mb.) Similarly, the predicted $(p,p')$ cross sections were about 30% smaller than the measured ones. For both $(\alpha,\alpha')$ and $(p,p')$, however, the predicted $2^+$ cross sections were in satisfactory agreement with experiment.

Only a small modification of the $0^+$ transition density is needed in order to reproduce the observed scattering. For example, a 3% stretching of the Tassie density $\rho_{\rm tr}^T$ of Eq. (9),

$$\rho_{\rm tr}(r)=\rho_{\rm tr}^T(r/1.03)\,,$$

is sufficient to give about twice the $(\alpha,\alpha')$ cross sections for $^{208}$Pb. This stretching corresponds to moving the Tassie density outwards by about 0.2 fm in the surface. (It is only the outer part of the density which contributes to the folded potential; for example, setting the density [Eq. (9)] equal to zero inside the node ($\rho_{\rm tr}=0$ for $r<6.2$ fm for $^{208}$Pb) has no effect on the folded potential near the strong absorption radius, while setting it equal to zero inside the outer maximum ($r=7$ fm for $^{208}$Pb) has only a few percent effect on the folded potential.) It is interesting to note that a generator coordinate method calculation[26,27] of the giant monopole transition density gives significantly larger values than does the RPA or the Tassie model in the nuclear surface.

The possible deficiency of the Tassie density for the GMR has been noted[28] in folding model analyses of $^{208}$Pb$(\alpha,\alpha')$ at energies of 100 to 172 MeV. In this case a real Gaussian interaction was used which was not constrained to fit the observed elastic scattering; Woods-Saxon potentials were used for the distorted waves. Although their interaction $v_{N\alpha}$ is real, its volume integral per nucleon, 446 MeV fm$^3$, is similar to the modulus of ours for $^{208}$Pb (Table III), 489 MeV fm$^3$; its range is a little longer, $\alpha=2.07$ fm compared to our 1.94 fm. Consequently it can be expected to give rather similar inelastic cross sections.

These authors found that use of the Tassie transition density underestimated their observed GMR cross sections by approximately a factor of 2. They attempted to resolve this discrepancy by adding a term to the transition density. This term corresponds to an oscillation in the surface thickness of the ground state density.[29] By choosing the appropriate sign and varying the strength of this term, larger cross sections can be obtained. These authors found an improved fit to the angular distribution of the GMR excitation with 90% depletion of the EWSR.

Recent RPA calculations[30] of the GMR show the transition density to be smaller than the Tassie model near the outer peak but larger at larger radii. It remains to be seen whether this effect is sufficiently large to explain our discrepancies.

## IV. CONCLUSIONS

We have presented the results of measurements of the excitation by 152-MeV alpha particles of the giant monopole and quadrupole resonances as well as the excitation of low-lying $2^+$ and $3^-$ states for several targets from $^{46}$Ti to $^{208}$Pb. For all the targets we have studied, the ratio of continuum to giant resonance peak cross section is nearly one, larger than for lower-energy alpha scattering. Such an enhancement in the resonance contributes to a more certain extraction of the shapes, positions, and strengths of the giant resonance peaks.

Based on the clear appearance of two peaks in the $^{208}$Pb giant resonance spectra (and from other data[3,4] on $^{144}$Sm) we have assumed that an asymmetry on the high excitation energy side of the giant resonance peak indicates the presence of a second resonance. We cannot demonstrate that the asymmetry is not in fact part of a single GQR peak. Small angle $(\alpha,\alpha')$ measurements[3] using lower energy alphas have made a convincing argument that two separate resonance peaks are indeed present for $^{144}$Sm and $^{208}$Pb. Our objective was to extend the "two resonance" assumption to lighter nuclei where lower-energy $(\alpha,\alpha')$ measurements are difficult and where the $(p,p')$ measurements are possibly compromised by GDR excitation. The results of our analysis presented in Tables I and V are consistent with the existence of a GMR in all the nuclei studied other than $^{46}$Ti, in agreement with previous $(\alpha,\alpha')$,[2,3] $(p,p')$,[4] and $(^3\mathrm{He},^3\mathrm{He}')$ (Ref. 5) measurements. Our analysis has been further substantiated by recent small angle $(\alpha,\alpha')$ measurements on $^{116}$Sn and $^{90}$Zr (Ref. 3, Rozsa *et al.*).

We show in Fig. 9 the excitation energy of the GMR from our measurements and for previous measurements. The solid curve is the systematic energy $80A^{-1/3}$ MeV, which agrees very well with all of the data. If the compressibility of nuclear matter is given by the liquid drop expression

$$k_\infty=\frac{3R^2m}{\hbar^2\pi^2}[E_{(0^+)}]^2\,, \tag{17}$$

a value of $k_\infty\sim200$ MeV is deduced from the energy dependence $80A^{-1/3}$ MeV with $R=1.2A^{1/3}$ fm. Within the correctness of the DWBA model used, the results given in Table V show that essentially all of the $T=0$, $L=0$, EWSR is accounted for in

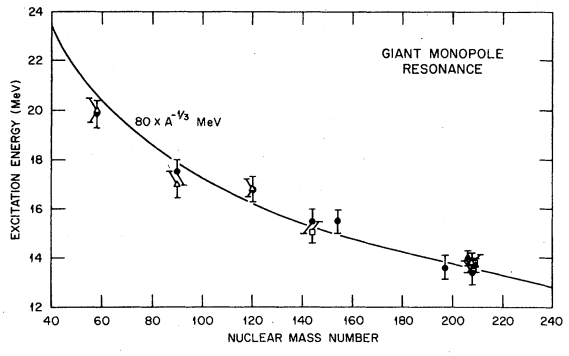


FIG. 9. Excitation energy (MeV) of the GMR for nuclei in which observations have been made. Open triangles—present results; circles—60 MeV $(p,p')$, Ref. 4; closed squares—96 MeV $(\alpha,\alpha')$, Ref. 3; closed triangles—120 MeV $(\alpha,\alpha')$, Ref. 2. The solid curve represents the energy $80A^{-1/3}$ MeV.

nuclei with $A \gtrsim 90$. However, for $^{58}$Ni only ~30% is observed and for $^{46}$Ti no evidence is found for monopole strength localized near $80A^{-1/3}$ MeV. A similar result was obtained for $^{40}$Ca from $(p,p')$ (Ref. 4) and $(^3\text{He},^3\text{He}')$ (Ref. 31) measurements.

The inelastic data were analyzed both with a conventional deformed potential model and with a folded potential model using Tassie transition densities. The alpha-nucleon interaction for the latter model was deduced from fits to elastic data. Good agreement was obtained for both the low-lying states and the GQR states; the strengths deduced are generally in good agreement with other measurements. The shape of measured angular distributions for the GMR excitations are well reproduced by both models, but the deduced transition strengths differ significantly. Comparison of the data with the deformed potential model yields monopole strengths which exhaust about 100% of the EWSR for $^{120}$Sn and $^{208}$Pb, 80% for $^{90}$Zr, and 40% for $^{58}$Ni. This reduction for the lighter nuclei agrees with earlier studies.[4] However the folding model predicts monopole cross sections smaller by as much as a factor of 2 for a given percentage of the EWSR, so that more than 100% of the EWSR is required to fit the measurements. We suggest that this is due to a deficiency in the transition density obtained from the Tassie model. The scattering in these cases is very sensitive to the magnitude of the tail of this density. Consequently, measurements of this type provide a sensitive test of models for the GMR.

## ACKNOWLEDGMENTS

We would like to thank the technical staff of IUCF for efficient cyclotron operation and assistance in preparation of the experimental apparatus. Oak Ridge National Laboratory is operated by Union Carbide Corporation under Contract No. W-7405-eng-26 with the U. S. Department of Energy. The work of A.D.B., G.T.E., W.P.J., and D.W.M. was supported in part by NSF.

[1] F. E. Bertrand, Annu. Rev. Nucl. Sci. 26, 457 (1976).
[2] M. H. Harakeh, K. van der Borg, T. Ishimatsu, H. P. Morsch, A. van der Woude, and F. E. Bertrand, Phys. Rev. Lett. 38, 676 (1977); M. N. Harakeh, Nucl. Phys. A327, 373 (1979).
[3] D. H. Youngblood, C. M. Rozsa, J. M. Moss, D. R. Brown, and J. D. Bronson, Phys. Rev. Lett. 39, 1188 (1977); C. M. Rozsa, D. H. Youngblood, J. D. Bronson, Y.-W. Lui, and U. Garg, Phys. Rev. C 21, 1252 (1980).
[4] F. E. Bertrand, G. R. Satchler, D. J. Horen, and A. van der Woude, Phys. Lett. 80B, 198 (1979).
[5] M. Buenerd, C. Bonhomme, D. Lebrun, P. Martin, J. Chauvin, G. Duhamel, G. Perrin, and P. de Saintignon, Phys. Lett. 84B, 305 (1979).
[6] H. P. Morsch, M. Rogge, P. Turek, C. Sükösd, and C. Mayer-Boricke, Phys. Rev. C 20, 1600 (1979).
[7] For a review of such recent work see: A. van der Woude, *Proceedings of the Giant Multipole Resonance Topical Conference, Oak Ridge,* edited by F. E. Bertrand (Harwood Academic, New York, 1980), p. 65.
[8] A. Kiss, C. Mayer-Boricke, M. Rogge, P. Turke, and S. Wiktar, Phys. Rev. Lett. 37, 1188 (1976).
[9] J. M. Moss, D. H. Youngblood, C. M. Rozsa, D. R. Brown, and J. D. Bronson, Phys. Rev. Lett. 37, 816 (1976).
[10] K. van der Borg, thesis, University of Groningen, 1979 (unpublished).
[11] D. A. Goldberg, S. M. Smith, H. G. Pugh, P. G. Roos, and N. S. Wall, Phys. Rev. C 7, 1938 (1973); D. A. Goldberg, S. M. Smith, and G. F. Burdzik, *ibid.* 10, 1362 (1974); P. L. Roberson, D. A. Goldberg, N. S. Wall, L. W. Woo, and H. L. Chen, Phys. Rev. Lett. 42, 54 (1979).
[12] I. Brissaud, B. Tatischeff, L. Bimbot, V. Comparat, and A. Willis, Phys. Rev. C 6, 595 (1972).
[13] R. C. Barrett and D. F. Jackson, *Nuclear Sizes and Structure* (Clarendon, Oxford, 1977).
[14] G. R. Satchler and W. G. Love, Phys. Rep. 55C, 183 (1979).
[15] J. W. Negele, Phys. Rev. C 1, 1260 (1970); 9, 1054 (1974).
[16] A. Chaumeaux, V. Layly, and R. Schaeffer, Ann. Phys. (N.Y.) 116, 247 (1978); L. Ray, Phys. Rev. C 19, 1855 (1979).
[17] J. Gils, H. Rebd, J. Buschmann, H. Klewe-Nechenius, G. P. Nowicki, and W. Nowatzke, Z. Phys. A 279, 55 (1976).
[18] A. M. Bernstein, in *Advances in Nuclear Physics,* edited by M. Baranger and E. Vogt (Plenum, New York, 1969), Vol. 3.
[19] G. R. Satchler, in *Elementary Modes of Excitation in Nuclei,* edited by A. Bohr and R. A. Broglia (North-Hol-

land, Amsterdam, 1977).
[20]E. C. Halbert, J. B. McGrory, G. R. Satchler, and J. Speth, Nucl. Phys. A245, 189 (1975); J. Wambach, F. Osterfeld, J. Speth, and V. A. Madsen, *ibid.* A324, 77 (1979).
[21]E. I. Kao and S. Fallieros, Phys. Rev. Lett. 25, 827 (1970); H. Ui and T. Tsukamoto, Prog. Theor. Phys. 51, 1377 (1974).
[22]D. H. Youngblood, J. M. Moss, C. M. Rozsa, J. D. Bronson, A. D. Bacher, and D. R. Brown, Phys. Rev. C 13, 994 (1976).
[23]A. M. R. Joye, A. M. Baxter, M. P. Fewell, D. C. Kean, and R. H. Spear, Phys. Rev. Lett. 38, 807 (1977).
[24]S. Raman, W. T. Milner, C. W. Nestor, and P. H. Stelson, Proceedings of the International Conference on Nuclear Structure, Tokyo, 1980 (unpublished), and private communication.
[25]C. F. Clement, A. M. Lane, and J. R. Rook, Nucl. Phys. 66, 273 (1965); G. R. Satchler, *ibid.* A195, 1 (1972).
[26]G. A. Rinker and J. Speth, Nucl. Phys. A306, 360 (1978).
[27]S. Krewald, R. Rosenfelder, J. E. Galonska, and A. Faessler, Nucl. Phys. A269, 112 (1976).
[28]H. P. Morsch, Proceedings of the European Physical Society Conference on Large Amplitude Collective Nuclear Motions, Keszthely, Hungary, 1980, edited by A. Kiss, J. Németh, and J. Zimányi (unpublished), p. 99.
[29]G. R. Satchler, Nucl. Phys. A100, 481 (1970).
[30]F. Serr, G. Bertsch, and J. P. Blaizot, Phys. Rev. C 22, 922 (1980).
[31]T. Yamagata, K. Iwamoto, S. Kishimoto, B. Saeki, K. Yuasa, M. Tanaka, T. Fukuda, K. Okada, I. Miura, M. Inoue, and H. Ogata, Phys. Rev. Lett. 40, 1628 (1978).